Title

Deep Learning Synthetic Strain: Quantitative Assessment of Regional Myocardial Wall Motion at MRI.

Journal

Radiology. Cardiothoracic imaging, 5(3)

ISSN

2638-6135

Authors

Masutani, Evan M
Chandrupatla, Rahul S
Wang, Shuo
et al.

Publication Date

2023-06-01

DOI

10.1148/ryct.220202

Peer reviewed

Radiology: Cardiothoracic Imaging

ORIGINAL RESEARCH

Deep Learning Synthetic Strain: Quantitative Assessment of Regional Myocardial Wall Motion at MRI

Evan M. Masutani, PhD • Rahul S. Chandrupatla, BS • Shuo Wang, PhD • Chiara Zocchi, MD • Lewis D. Hahn, MD • Michael Horowitz, MD, PhD • Kathleen Jacobs, MD • Seth Kligerman, MD • Francesca Raimondi, MD • Amit Patel, MD • Albert Hsiao, MD, PhD

From the Departments of Bioengineering (E.M.M.) and Radiology (R.S.C., L.D.H., M.H., K.J., S.K., A.H.), University of California, San Diego, 9300 Campus Point Dr, MC 0841, La Jolla, CA 92037-0841; Department of Medicine, University of Virginia, Charlottesville, Va (S.W., A.P.); and Meyer Children's Hospital IRCCS, Cardiac Imaging Unit, Pediatric Cardiology, University of Florence, Florence, Italy (C.Z., F.R.). Received September 22, 2022; revision requested November 25; revision received March 7, 2023; accepted March 20. **Address correspondence to** A.H. (email: *hsiao@ucsd.edu*).

Supported by philanthropic grants from Microsoft's AI for Health program and Oracle for Research for computational resources used to train deep learning algorithms. E.M.M. supported by training grant funding from the Radiological Society of North America Medical Student Research Grant (grant no. RMS2120), the American Heart Association Predoctoral Fellowship (no. 20PRE35180166), the National Institutes of Health/National Institute of General Medical Sciences Medical Scientist Training Program (grant no. T32GM007198), and the National Heart, Lung, and Blood Institute (grant no. T32 HL105373). R.S.C. supported by training grant funding from the Altman Clinical and Translational Research Institute MedGap Program.

Conflicts of interest are listed at the end of this article.

Radiology: Cardiothoracic Imaging 2023; 5(3):e220202 • https://doi.org/10.1148/ryct.220202 • Content codes: AI CA MR

Purpose: To assess the feasibility of a newly developed algorithm, called *deep learning synthetic strain* (DLSS), to infer myocardial velocity from cine steady-state free precession (SSFP) images and detect wall motion abnormalities in patients with ischemic heart disease.

Materials and Methods: In this retrospective study, DLSS was developed by using a data set of 223 cardiac MRI examinations including cine SSFP images and four-dimensional flow velocity data (November 2017 to May 2021). To establish normal ranges, segmental strain was measured in 40 individuals (mean age, 41 years ± 17 [SD]; 30 men) without cardiac disease. Then, DLSS performance in the detection of wall motion abnormalities was assessed in a separate group of patients with coronary artery disease, and these findings were compared with consensus results of four independent cardiothoracic radiologists (ground truth). Algorithm performance was evaluated by using receiver operating characteristic curve analysis.

Results: Median peak segmental radial strain in individuals with normal cardiac MRI findings was 38% (IQR: 30%–48%). Among patients with ischemic heart disease (846 segments in 53 patients; mean age, 61 years ± 12; 41 men), the Cohen κ among four cardiothoracic readers for detecting wall motion abnormalities was 0.60–0.78. DLSS achieved an area under the receiver operating characteristic curve of 0.90. Using a fixed 30% threshold for abnormal peak radial strain, the algorithm achieved a sensitivity, specificity, and accuracy of 86%, 85%, and 86%, respectively.

Conclusion: The deep learning algorithm had comparable performance with subspecialty radiologists in inferring myocardial velocity from cine SSFP images and identifying myocardial wall motion abnormalities at rest in patients with ischemic heart disease.

Supplemental material is available for this article.

Cardiac MRI is the clinical reference standard for noninvasive evaluation of cardiac function because of its utility for completely visualizing the heart without ionizing radiation or dependence on sonographic windows (1–3). Ventricular volumetry and ejection fraction provide an assessment of global ventricular function but do not provide regional granularity. Clinical assessment of regional myocardial function largely remains a subjective visual task by expert readers (4–8). Though the degree of agreement among expert cardiac MRI readers has not been established, assessment for regional wall motion abnormalities is widely practiced clinically because it provides important cues for the diagnosis of multiple diseases (9–11), including ischemic heart disease.

Strain imaging techniques, first described in the 1980s (12), have the potential to provide granular measurements of regional myocardial function. Multiple methods have been developed, including myocardial tagging (12), displacement encoding with stimulated echoes (13), strain-encoded MRI (14), and harmonic phase (15) and phase-contrast velocity mapping (16,17). Each, however, requires acquisition of a dedicated imaging sequence and considerable postprocessing analysis. More recently, feature tracking strain methods have emerged as an approach for retrospective analysis of strain from cine steady-state free precession (SSFP) images (18–20), with multiple studies showing potential value in measurements of global strain. However, while echocardiographic studies have confirmed the relationship between regional speckle tracking strain and visual grades of myocardial function (21) or myocardial scar (22,23), feature tracking methods lack this evidence base. This may be the result of the limited reliability of feature tracking methods for assessing regional wall motion (23); these methods have shown widely varying ranges in healthy individuals (24) and poor agreement with established strain imaging techniques (25,26).

Deep learning methods, specifically convolutional neural networks (CNNs), have emerged as a powerful

Abbreviations

AUC = area under the receiver operating characteristic curve, CNN = convolutional neural network, DLSS = deep learning synthetic strain, 4D = four-dimensional, ICC = intraclass correlation coefficient, SSFP = steady-state free procession

Summary

A deep learning algorithm was able to infer myocardial velocities and quantify strain from cine steady-state free precession images to detect wall motion abnormalities in patients with ischemic heart disease, performing comparably with subspecialty radiologists.

Key Points

- Normal ranges for segmental myocardial strain and strain rate for the deep learning algorithm were measured in 40 individuals without known cardiac disease.
- Subspecialty radiologists showed moderate-to-substantial agreement for the detection of wall motion abnormalities across 846 myocardial segments in 53 patients with ischemic heart disease (Cohen κ, 0.60–0.78).
- Relative to the consensus of four subspecialty radiologists, the algorithm detected wall motion abnormalities in patients with ischemic heart disease at rest, with an area under the receiver operating characteristic curve of 0.90 and an accuracy, sensitivity, and specificity of 86%, 85%, and 86%, respectively.

Keywords

Neural Networks, Cardiac, MR Imaging, Ischemia/Infarction

technology for the analysis of biomedical image data and are capable of rapidly performing computational tasks. Applications of this technology in cardiac MRI include image classification (27), localization (28,29), segmentation (30–32), and image enhancement (33,34). Recent groups have proposed the application of deep learning methods to simplify the analysis of dedicated strain imaging techniques (35,36). However, a rate-limiting factor for such techniques requires a separate acquisition of strain image data.

We thus sought to develop an alternative strategy, which we call *deep learning synthetic strain* (DLSS), to enable the measurement of myocardial wall motion from cine SSFP images routinely acquired at clinical cardiac MRI. We applied this approach to first identify normal ranges for strain and strain rate in a sample of individuals without cardiac disease and used these data to establish thresholds for abnormal myocardial contraction. Finally, we evaluated the ability of DLSS to detect abnormalities in regional myocardial contraction in a sample of patients enriched for wall motion abnormalities, specifically those with catheter angiography–proven coronary artery disease.

Materials and Methods

Our Health Insurance Portability and Accountability Act–compliant study was performed with institutional review board approval, including waiver of informed consent, for the development of the algorithm and assessment of retrospective patient groups. We obtained written informed consent from healthy volunteers according to a separate institutional review board protocol for MRI examinations of the volunteers.

Algorithm Development and Training Data

DLSS was developed by training a CNN architecture to infer pixelwise myocardial velocity fields from short-axis cine SSFP image series. Details are provided in Appendix S1. These velocity fields were then used to calculate pixelwise myocardial strain rate and strain. To train this CNN, myocardial velocity fields from four-dimensional (4D) flow MRI were coregistered to cine SSFP images by using in-house custom software to provide ground truth for velocity field inference. We emphasize that this algorithm requires only short-axis cine SSFP images for execution, and 4D flow velocity fields were required only for algorithm training.

To establish data for deep learning algorithm development, we retrospectively collected a convenience sample of 223 cardiac MRI examinations in 219 patients, which included short-axis cine SSFP and 4D flow as part of routine clinical examinations at our institution between November 2017 and May 2021 (Table S1). Four-dimensional flow and short-axis cine SSFP images were acquired during the same examination for each patient with full left ventricle coverage, allowing for coregistration of images. Four-dimensional flow MRI sections were corrected for phase error (Cardio AI, version 29.4.0; Arterys). Four-dimensional flow velocities were then linearly resampled and coregistered with cine SSFP images by the lead author (E.M.M.), a 6th-year MD-PhD student, using custom in-house software developed in Python. Left ventricular myocardial segmentations were performed using commercial software (Cardio AI, version 29.4.0; Arterys) (37) and incorporated into algorithm training.

Data were divided into training and validation data sets by examination. Ninety percent of examinations (602 short-axis sections from 201 examinations) were allocated to the training set, and 10% of examinations (65 sections from 22 examinations) were allocated to the validation set for CNN optimization. Training data were augmented by in-plane rotation at 15° increments and variable adjustments of image contrast, including intensity thresholding and normalization.

Neural Network Architecture

The lead author designed and trained a CNN architecture, based on a modified three-dimensional U-Net architecture (34), to infer spatiotemporal myocardial segmentations and velocity fields from short-axis cine SSFP images (Fig 1, Movie 1). The CNN was trained on an NVIDIA DGX-A100 graphics processing unit server comprising A100 graphics processing units. The CNN takes images from the entire cardiac cycle and returns the in-plane myocardial velocity field and myocardial segmentations for each time frame, which are postprocessed to yield strain rate and strain fields. These are further decomposed into radial and circumferential components. Additional details regarding CNN architecture and data postprocessing can be found in Figure S1. The code for our CNN is available on request via GitHub *(https://github.com/AiDALabUCSD/DLSS)*.

Data Acquisition

MRI examinations were performed with either a 1.5-T MRI scanner (Signa HDxt; GE Healthcare) or a 3.0-T MRI scan-

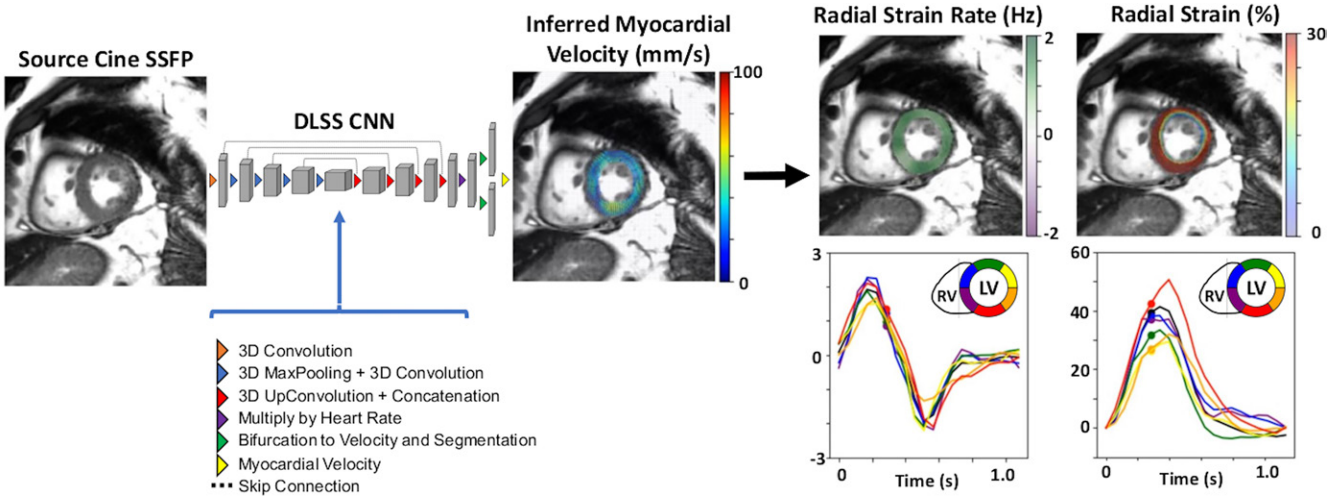

Figure 1: Images show overview of the deep learning synthetic strain (DLSS) approach. A convolutional neural network (CNN) was trained to infer myocardial velocities from a series of cine steady-state free precession (SSFP) images. Training data included coregistered myocardial velocities from cardiac MRI examinations in 219 patients who underwent four-dimensional flow as part of their clinical examination. The inferred myocardial velocities were then used to calculate myocardial strain rate and strain maps, which are superimposed on the source SSFP images for quantification and visual interpretation. This example shows short-axis SSFP images in a 58-year-old male patient with normal cardiac MRI findings. LV = left ventricle, RV = right ventricle, 3D = three-dimensional.

ner (Discovery MR750 DV26; GE Healthcare). All examinations employed a standard 32-channel phased-array coil. Four-dimensional flow MRI was performed at 3.0 T following administration of intravenous gadolinium-based contrast agent (gadobenate dimeglumine, 0.15 mmol per kilogram of body weight) and employed respiratory self-navigation, compressed sensing, and parallel imaging reconstruction (38). Additional scanning parameters for algorithm development and independent testing data sets are listed in Tables S2 and S3, respectively.

Segmental and Global Strain in Individuals with Normal Cardiac MRI Findings

To identify normal segmental and global strain ranges for the DLSS technique, short-axis cine SSFP series were obtained in a separate sample of 40 individuals not included in algorithm training or validation sets, composed of 21 healthy volunteers and 19 patients with normal cardiac MRI findings (referred for iron deposition screening or arrhythmogenic right ventricular cardiomyopathy) from February 2015 and October 2021. Normal cardiac MRI findings were defined as normal ventricular volume and function and an absence of delayed enhancement. Additionally, three board-certified cardiothoracic radiologists (M.H., L.D.H., K.J.) independently reviewed all MRI studies and confirmed the absence of any wall motion abnormalities in this group. Images were processed with DLSS to yield segmental and global strain measurements. To provide additional reference points, we measured per-section peak radial and circumferential strain by using two commercially available feature tracking software programs, Medis (version 4.0.56.4; Medis Medical Imaging Systems) and suiteHEART (version 5.0.3; NeoSOFT) (19). Image file incompatibility errors occurred with Medis in seven of the 40 individuals, excluding those individuals from this analysis. All 40 individuals were successfully analyzed using the suiteHEART software and were included in this analysis. We assessed agreement between software programs by using the Pearson correlation coefficient.

Assessment of Wall Motion Abnormalities in Patients with Ischemic Heart Disease

To assess the utility of DLSS for identifying segmental wall motion abnormalities, short-axis cine SSFP images in a separate sample of 53 patients with catheter angiography–proven ischemic heart disease were curated from those who underwent MRI examinations performed between September 2014 and December 2020 (Table S4), based on retrospective chart review of patients who also underwent coronary catheterization. Only patients with greater than 70% stenosis in at least one of the left main, left anterior descending, left circumflex, or right coronary arteries were included. None of these overlapped with patients used in algorithm development. We calculated strain by using DLSS and partitioned it into 16 American Heart Association segments, excluding the apical segment, for a total of 848 segments.

To establish a reference standard for the presence of wall motion abnormalities, four board-certified cardiothoracic radiologists with 14 (S.K.), 2 (M.H.), 2 (L.D.H.), and 3 (K.J.) years of postfellowship experience independently graded each segment on a 1–4 scale as follows: 1 = normal, 2 = hypokinetic, 3 = akinetic, and 4 = dyskinetic. Radiologists were provided solely short-axis cine SSFP images and were blinded to all other clinical and demographic information. Because few dyskinetic segments were identified in this group, we pooled dyskinetic and akinetic segments for analysis. Segmental wall motion scores for all four radiologists were averaged (mean) to serve as consensus ground truth for DLSS assessment. Two of 848 segments were excluded by readers because off-resonance artifact precluded interpretation of wall motion. To further analyze the ability of DLSS to identify segments with ischemic disease, two board-certified cardiothoracic radiologists with 8 (A.H.) and 3 (K.J.) years of

Table 1: Study Sample Characteristics

Parameter	Normal Volunteer MRI Findings (n = 21)	Normal Clinical MRI Findings (n = 19)	Ischemic Heart Disease (n = 53)
Male-to-female ratio	18:3	12:7	41:12
Age (y)	29 ± 5	55 ± 15	61 ± 12
BMI (kg/m^2)	24.1 ± 2.9	28.1 ± 6.4	27.2 ± 4.9
BSA (m^2)	1.87 ± 0.18	1.89 ± 0.30	1.94 ± 0.23
Heart rate (beats/min)	66 ± 12	66 ± 10	75 ± 21
1.5-T/3.0-T field strength ratio	0:21	3:16	38:15

Note.—Continuous data presented as sample means ± SDs, categorical data as numbers of individuals. BMI = body mass index, BSA = body surface area.

postfellowship experience, also blinded to DLSS algorithm results, classified the presence or absence of myocardial scar exceeding 50% of wall thickness in each myocardial segment.

Statistical Analysis

To assess interrater agreement among subspecialty cardiothoracic radiologists for grading of wall motion abnormalities, we calculated the Cohen κ coefficient and intraclass correlation coefficient (ICC) (39). κ values of 0.41–0.60 and 0.61–0.80 denoted moderate and substantial agreement, respectively (40). ICC values above 0.75 were considered excellent (41). To evaluate DLSS algorithm performance for detecting wall motion abnormalities, we generated receiver operating characteristic curves and reported the area under the receiver operating characteristic curve (AUC). The thresholds for discriminating normal from abnormal myocardial wall motion were set to the 25th and 75th percentiles of radial and circumferential strain, respectively, of the individuals with normal cardiac MRI findings. Thresholds for akinesis and dyskinesis were defined as 50% of this threshold. We also reported the mean and SD of DLSS-derived strain in segments with and without myocardial scar and determined statistical significance using the Student t test with a type I error threshold of 0.05 ($P < .05$).

Statistical analysis was performed using Python (version 3.7; Python Software Foundation), NumPy 1.21.5, SciPy 1.7.3, scikit-learn 0.23.2, pingouin 0.5.0, and Excel (version 2301; Microsoft).

Results

Study Sample Characteristics

Characteristics for the 21 healthy volunteers (mean age, 29 years ± 5 [SD]; 18 men) and 19 patients (mean age, 55 years ± 15; 12 men) with normal cardiac MRI findings are summarized in Table 1 and Appendix S1. The mean age of patients was higher than that of healthy volunteers ($P < .001$), with a greater number of men than women ($P = .001$). Fifty-three patients (mean age, 61 years ± 12; 41 men) with ischemic heart disease were included (Tables 1 and S4).

Ranges of Segmental Strain in Individuals with Normal Cardiac MRI Findings

Normal DLSS peak radial and circumferential strains for each segment are listed in Table 2. Peak radial strain for each segment is shown in Figure 2. Broadly, we note lower median peak radial strain in the anterior, anteroseptal, and inferoseptal segments. Peak radial strain was greater in apical segments. In contrast, we observed less variability in segmental peak circumferential strain across segments.

In the 21 healthy volunteers, the median peak radial strain averaged over all 16 American Heart Association segments was 35% (IQR: 27%–45%). Median peak global radial strain was 38% (IQR: 34%–40%). We observed similar values in an independent group of 19 patients with normal cardiac MRI findings, with median peak radial strain of 41% (IQR: 33%–49%) and median global radial strain of 40% (IQR: 38%–47%). Pooled median peak radial strain was 38% (IQR: 30%–48%), and median global radial strain was 39% (IQR: 36%–44%). We observed similar trends for peak circumferential strain (Table 2).

Statistical comparisons between peak radial and peak circumferential strain for both groups are provided in Table S5.

Comparison with Feature Tracking

To assess the relationship between strain measurements from DLSS and feature tracking, we computed per-section radial and circumferential strain by using each method in the same cohort of 40 individuals. For DLSS, median per-section radial and circumferential strains were 40% (IQR: 35%–45%) and −39% (IQR: −44% to −35%), respectively (Fig S2). For Medis, median radial, myocardial circumferential, and endocardial circumferential strains were 93% (IQR: 78%–107%), −21% (IQR: −23% to −18%), and −31% (IQR: −35 to −27%), respectively. For suiteHEART, median radial and circumferential strain were 65% (IQR: 54%–78%) and −16% (IQR: −18% to −15%), respectively. There was very weak–to-moderate correlation among methods for radial strain (r = 0.18 to 0.49), with the highest correlation between suiteHEART and DLSS for radial

Table 2: DLSS Peak Strain in Volunteers and Patients without Known Cardiac Disease

AHA Segment	Peak Radial Strain (%)			Peak Circumferential Strain (%)		
	Volunteers (n = 21)	Patients (n = 19)	Combined (n = 40)	Volunteers (n = 21)	Patients (n = 19)	Combined (n = 40)
1. Basal anterior	31 (27–38)	37 (32–41)	34 (28–41)	−28 (−35 to −22)	−41 (−48 to −34)	−34 (−42 to −26)
2. Basal anteroseptal	30 (25–35)	34 (29–43)	31 (27–38)	−33 (−38 to −26)	−36 (−47 to −31)	−34 (−41 to −30)
3. Basal inferoseptal	27 (23–32)	34 (26–40)	29 (25–38)	−43 (−49 to −26)	−42 (−51 to −34)	−42 (−50 to −34)
4. Basal inferior	48 (35–53)	49 (41–59)	48 (41–54)	−39 (−55 to −28)	−37 (−48 to −30)	−28 (−54 to −29)
5. Basal inferolateral	46 (40–52)	46 (37–54)	46 (38–53)	−38 (−48 to −31)	−42 (−48 to −36)	−40 (−47 to −34)
6. Basal anterolateral	40 (34–43)	40 (33–48)	40 (34–46)	−35 (−39 to −32)	−39 (−46 to −30)	−36 (−44 to −31)
7. Midventricular anterior	25 (21–30)	32 (28–35)	29 (25–33)	−28 (−36 to −21)	−38 (−45 to −32)	−36 (−39 to −27)
8. Midventricular anteroseptal	27 (20–30)	33 (28–40)	29 (25–38)	−28 (−31 to −23)	−32 (−43 to −27)	−30 (−37 to −26)
9. Midventricular inferoseptal	28 (23–34)	38 (33–45)	34 (28–41)	−36 (−42 to −28)	−41 (−51 to −29)	−40 (−46 to −29)
10. Midventricular inferior	50 (43–58)	51 (45–65)	51 (44–61)	−43 (−49 to −34)	−47 (−56 to −33)	−45 (−54 to −33)
11. Midventricular inferolateral	46 (39–58)	49 (43–56)	48 (40–57)	−48 (−54 to −37)	−49 (−57 to −42)	−49 (−55 to −39)
12. Midventricular anterolateral	33 (31–38)	42 (32–47)	36 (31–45)	−29 (−37 to −23)	−37 (−46 to −29)	−34 (−41 to −26)
13. Apical anterior	25 (19–32)	38 (33–48)	32 (24–45)	−30 (−37 to −26)	−42 (−48 to −34)	−36 (−46 to −27)
14. Apical septal	23 (20–32)	38 (29–46)	31 (22–39)	−32 (−42 to −25)	−42 (−47 to −37)	−39 (−46 to −30)
15. Apical inferior	50 (45–69)	51 (46–61)	50 (45–67)	−44 (−51 to −34)	−47 (−63 to −42)	−45 (−62 to −37)
16. Apical lateral	56 (40–64)	49 (43–57)	50 (41–62)	−39 (−51 to −34)	−44 (−52 to −39)	−41 (−52 to −36)
Pooled segments	35 (27–45)	41 (33–49)	38 (30–48)	−35 (−44 to −27)	−41 (−49 to −33)	−38 (−30 to −47)

Note.—Data for all myocardial segments are presented as medians, with IQRs in parentheses. AHA = American Heart Association, DLSS = deep learning synthetic strain.

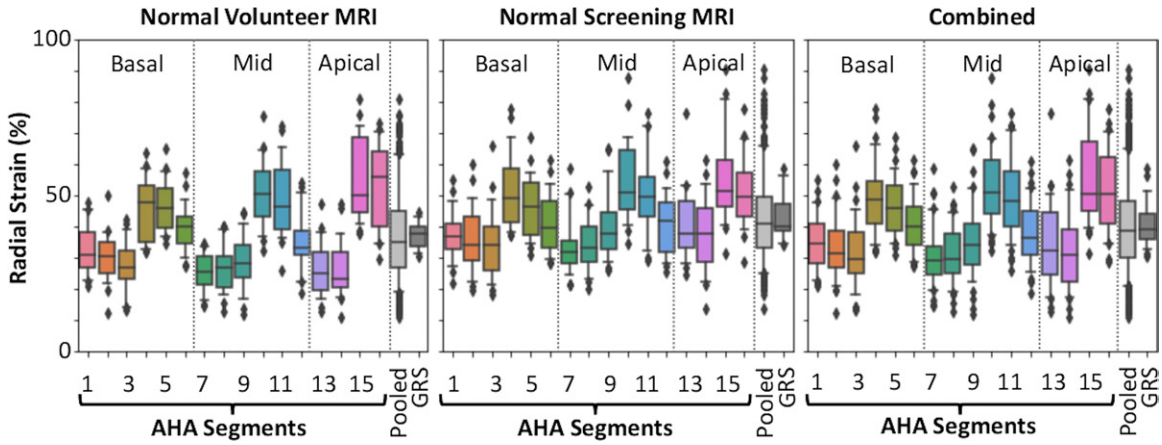

Figure 2: Graphs show the distribution of peak radial strain in healthy volunteers and in patients with normal clinical cardiac MRI findings. Deep learning synthetic strain (DLSS) algorithm estimates of radial strain were computed in 21 healthy volunteers and 19 patients with normal cardiac MRI findings who had been referred for iron deposition screening or for family history of arrhythmogenic right ventricular cardiomyopathy. Both groups showed a similar distribution of DLSS-estimated peak radial strain. Boxes represent the IQRs (25th–75th percentiles), and the horizontal lines inside the boxes represent the median values of each parameter. Whiskers indicate the 2.5th and 97.5th percentiles. ▪▪▪ indicates outliers. AHA = American Heart Association, GRS = global radial strain.

strain (Table S6). There was moderate-to-strong correlation among methods for circumferential strain (r = 0.48 to 0.76), which was highest between suiteHEART and Medis for circumferential strain (Table S6).

Reader Agreement for Ischemic Wall Motion Abnormalities

Table 3 shows the interobserver agreement among the four cardiothoracic radiologists. For classification of normal versus abnormal segments, Cohen κ ranged from 0.60 to 0.78, indicating moderate-to-substantial interobserver agreement. ICC(2,k) was 0.96 (95% CI: 0.93, 0.98). For classification of normal versus hypokinetic versus akinetic or dyskinetic segments, Cohen κ ranged from 0.52 to 0.64, indicating moderate-to-substantial interobserver agreement. ICC(2,k) was 0.97 (95% CI: 0.95, 0.98). Notably, the maximum difference between any two readers at any segment was one grade.

Table 3: Interrater Cohen κ for Identification of Segmental Wall Motion Abnormalities

Cohen κ Normal vs Abnormal Segments				
Reader	Reader 1	Reader 2	Reader 3	Reader 4
1		0.75	0.72	0.60
2			0.78	0.62
3				0.60
Cohen κ Normal vs Hypokinetic vs Akinetic or Dyskinetic Segments				
Reader	Reader 1	Reader 2	Reader 3	Reader 4
1		0.64	0.61	0.52
2			0.62	0.54
3				0.52

Deep Learning Detection of Wall Motion Abnormalities

In the DLSS schematic diagram (Fig 1), we show an example case of a 58-year-old man with normal cardiac MRI findings who initially presented with fatigue and dyspnea on exertion. The patient was subsequently found to have no obstructive coronary artery disease at coronary artery catheterization. DLSS radial strain rate curves were relatively uniform across all myocardial segments, with peak segmental strain rates ranging from 1.47 Hz to 2.27 Hz. DLSS radial strain curves were also relatively uniform across all myocardial segments, with peak segmental values ranging from 29% to 47%.

In contrast, a 66-year-old man with a history of coronary artery disease and ST-segment elevation myocardial infarction presented with intermittent chest pressure and underwent cardiac MRI 3 days after acute presentation (Fig 3, Movie 2). Cardiac MRI performed at 1.5 T showed reduced global function (left ventricular ejection fraction, 25%). DLSS showed markedly reduced strain rate and strain in the basal anteroseptal and inferoseptal segments in addition to multiple midventricular and apical segments (not shown) corresponding to the left anterior descending territory. Peak radial strain of the anteroseptal and inferoseptal segments were 8.4% and −2.2%, respectively, far below the normal range. Peak radial strain of the remaining segments ranged from 32% to 42%, within the normal range. Following administration of intravenous contrast agent, we observed a perfusion defect and transmural delayed enhancement in the septal wall. Findings at catheter angiography confirmed complete occlusion of the mid left anterior descending artery.

Figure 4 shows receiver operating characteristic curves for DLSS detection of segmental wall motion abnormalities. Using fixed thresholds of peak radial strain to identify wall motion abnormalities yielded an AUC of 0.90 (Fig 4A). Similarly, using segment-specific percentile thresholds of peak radial strain yielded an AUC of 0.90. At peak radial strain threshold of 30%, DLSS had 86% (95% CI: 85%, 87%) sensitivity, 85% (95% CI: 79%, 91%) specificity, and 86% (95% CI: 85%, 87%) accuracy (Table 4). In comparison, expert reader performance relative to the consensus of the remaining three readers ranged from 84% to 97% for sensitivity, 78% to 90% for specificity, and 85% to 93% for accuracy (Fig 4B). For discrimination of hypokinetic versus akinetic or dyskinetic segments using a peak radial strain threshold of 15%, DLSS had 90% (95% CI: 87%, 93%) sensitivity, 66% (95% CI: 65%, 67%) specificity, and 72% (95% CI: 71%, 73%) accuracy. Peak circumferential strain was generally less reliable for detecting wall motion abnormalities than was peak radial strain and had an AUC of 0.87. For identification of any wall motion abnormalities, DLSS peak circumferential strain threshold of −30% had 83% (95% CI: 82%, 84%) sensitivity, 77% (95% CI: 72%, 82%) specificity, and 82% (95% CI: 81%, 83%) accuracy. For discrimination of hypokinetic versus akinetic or dyskinetic segments, fixed circumferential strain cutoff of −15% yielded 73% (95% CI: 71%, 75%) sensitivity, 72% (95% CI: 70%, 74%) specificity, and 72% (95% CI: 70%, 74%) accuracy.

We additionally investigated the utility of DLSS for identifying segments with myocardial scar. Of the 846 segments evaluated in patients with ischemic heart disease, 43% (364 of 846 segments) had delayed enhancement exceeding 50% of myocardial wall thickness. Mean DLSS radial strain was significantly lower in segments with delayed enhancement involving greater than 50% of myocardial wall thickness ($P < .001$). DLSS radial strain in normal segments was 28% ± 18 and in segments with myocardial scar was 18% ± 12. DLSS radial strain was able to predict the presence of myocardial scar exceeding 50% of the myocardial wall thickness, with an AUC of 0.68.

Potential Applications of DLSS beyond Ischemic Heart Disease

To further assess the potential of DLSS in detecting abnormal wall motion beyond the group of patients with ischemic heart disease, we executed the algorithm on two additional patients.

The first was a 55-year-old man who presented with cardiac arrest and who had been diagnosed with viral myocarditis 4 months prior to undergoing cardiac MRI. The patient was referred to MRI to assess scar for potential implantable cardioverter defibrillator placement and was found to have normal cardiac MRI findings with no delayed enhancement or edema. However, DLSS detected global hypokinesis with

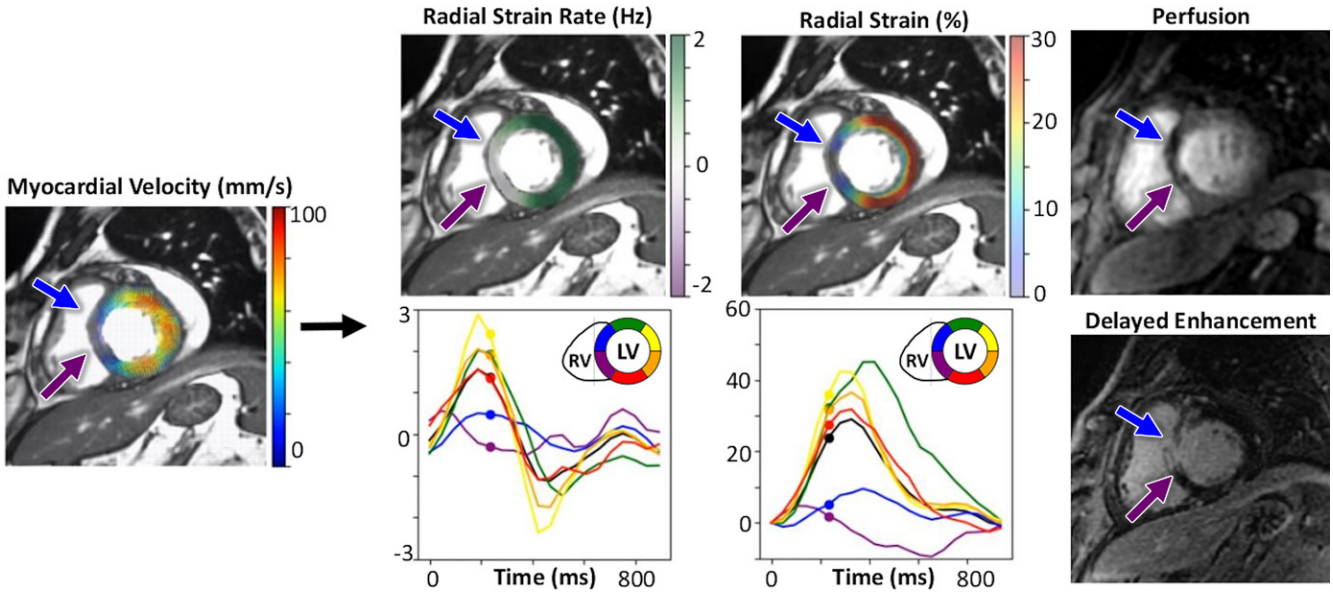

Figure 3: Example case of a 66-year-old man with catheter angiography–proven left anterior descending coronary artery occlusion. The images show focal wall motion abnormality of the anteroseptal (blue arrow) and inferoseptal (purple arrow) walls with decreased peak radial strain and strain rate. Corresponding strain and strain rate curves show the severity of this abnormality relative to the other myocardial segments in the same section. Following intravenous contrast agent administration, the septal wall shows a matching perfusion defect and transmural delayed enhancement, indicating myocardial ischemia and infarction. LV = left ventricle, RV = right ventricle.

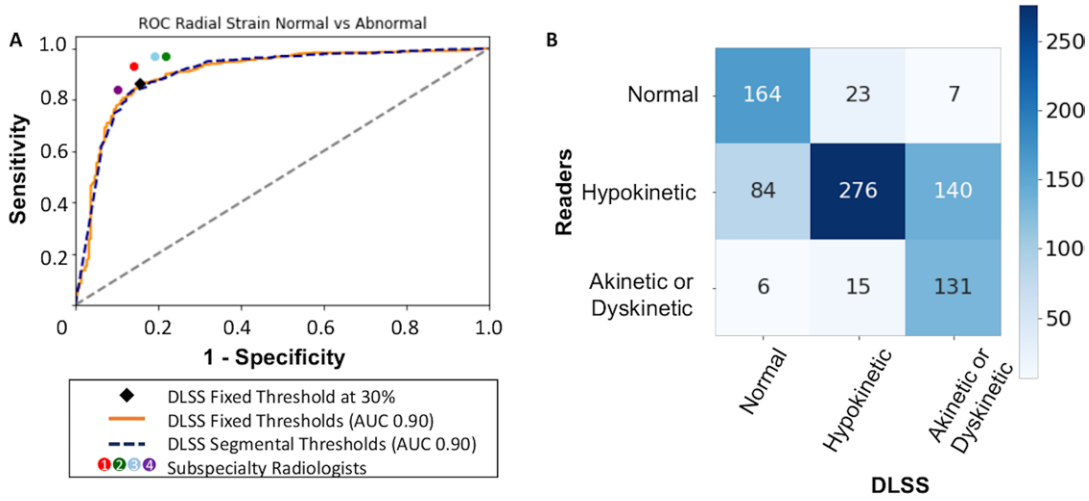

Figure 4: Performance of deep learning synthetic strain (DLSS) in detecting segmental wall motion abnormalities. **(A)** Receiver operating characteristic (ROC) curves for discrimination of normal from abnormal (hypokinetic, akinetic, dyskinetic) wall motion, relative to the consensus of four subspecialty readers. Orange line shows classification performance of DLSS when using fixed peak radial strain values as cutoffs (area under the ROC curve [AUC] = 0.90). Black diamond marks the location of the fixed peak radial strain threshold of 30% on the ROC curve. Dashed blue line shows classification performance of DLSS when using peak radial strain percentiles as cutoffs (AUC = 0.90). The performances of each reader relative to the average of the other readers are shown in the colored dots. **(B)** Confusion matrix for the performance of DLSS in discriminating wall motion abnormalities, relative to the average of four readers.

marked hypokinesis at the mid anteroseptal and anterior segments, with peak radial strains of 15% and 19%, respectively (Fig 5, Movie 3). Subsequent review of the delayed enhancement images showed subtle mesocardial delayed enhancement at the mid anteroseptal wall. After requesting to perform a second review of short-axis cine SSFP images from this patient without clinical history, readers 1, 2, and 3 interpreted the midventricular sections as globally hypokinetic and did not perceive additional focal wall motion abnormality. Reader 4 noted additional focal hypokinesis of the mid anterior wall, corresponding with reduced strain detected by DLSS.

The second patient, a 54-year-old man who presented with cardiac arrest, was referred for cardiac MRI to evaluate for myocardial scar and viability. The cardiac MRI findings were initially interpreted with no wall motion abnormalities or delayed enhancement. Catheter angiography findings were also unremarkable. However, DLSS detected marked dissociation between

Table 4: DLSS Performance Using Fixed Peak Strain Cutoffs

Task	Metric	Cutoff (%)	Sensitivity (%)	Specificity (%)	Accuracy (%)
Normal vs abnormal segments	Fixed peak radial strain	30	86 (85, 87)	85 (79, 91)	86 (85, 87)
	Fixed peak circumferential strain	−30	83 (82, 84)	77 (72, 82)	82 (81, 83)
Hypokinetic vs akinetic or dyskinetic segments	Fixed peak radial strain	15	90 (87, 93)	66 (65, 67)	72 (71, 73)
	Fixed peak circumferential strain	−15	73 (71, 75)	72 (70, 74)	72 (70, 74)

Note.—Values in parentheses are 95% CIs. A 30% peak radial strain corresponds to the 25th percentile of peak radial strain measurements in individuals without known cardiac disease. A −30% peak circumferential strain corresponds to the 75th percentile of peak circumferential strain measurements in these individuals. DLSS = deep learning synthetic strain.

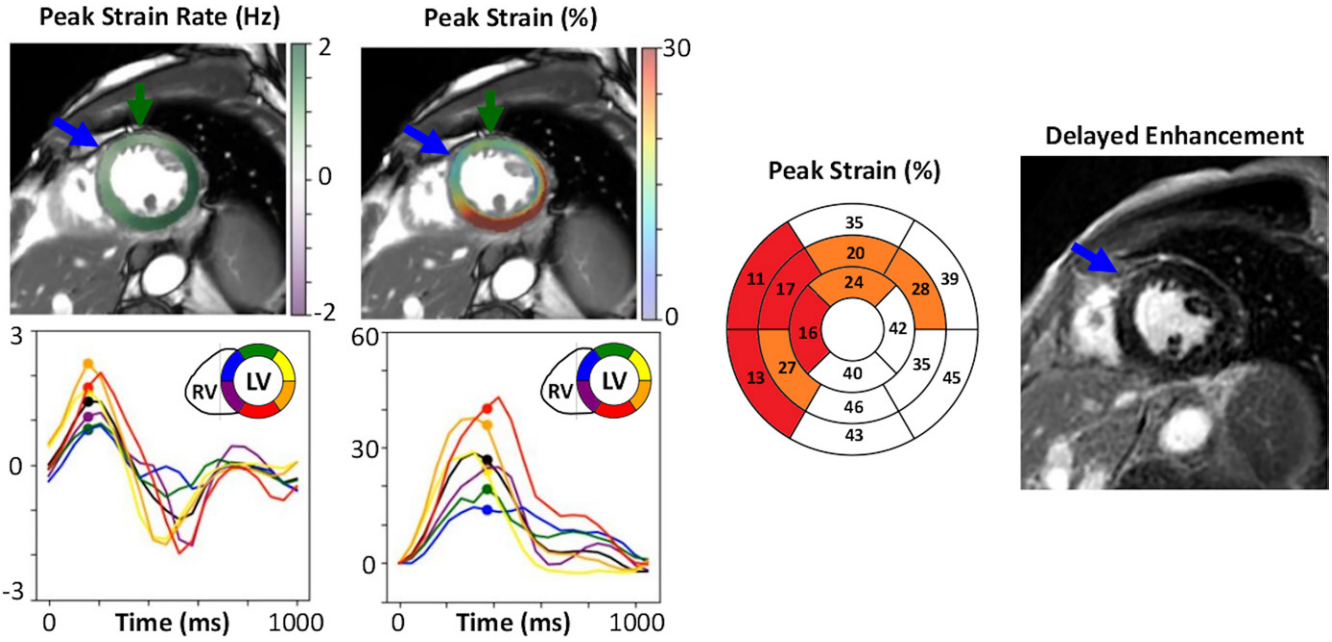

Figure 5: Images in a 55-year-old man with cardiac arrest 4 months prior with viral prodrome and presumed myocarditis with negative findings from myocardial biopsy. MR images show hypokinesis of the mid anteroseptal (blue arrow) and anterior (green arrow) wall evident on deep learning synthetic strain (DLSS)–derived peak radial strain rate and strain maps. Image after administration of intravenous contrast agent (image on right) shows only subtle mesocardial enhancement of the mid anteroseptal wall. Without DLSS strain maps, this case was initially interpreted clinically as having normal cardiac MRI findings. Peak segmental radial strain is shown in bull's-eye plot.

contraction of the septal and lateral walls (Fig 6, Movie 4). While the lateral wall contracted, the septal wall showed dyssynchronous relaxation with negative radial strain rate; while the lateral wall relaxed, the septal wall showed dyssynchronous contraction with positive radial strain rate. Electrocardiography helped confirm the presence of a complete left bundle branch block, which explains the pattern of dyssynchronous myocardial wall motion.

Discussion

In this study, we showed the potential of a deep learning algorithm to quantify strain and strain rate from routine short-axis cine SSFP MR images. To establish normal ranges for segmental radial and circumferential strain, we analyzed segmental strain in 16 American Heart Association segments in 40 individuals without known cardiac disease. We showed the potential of the deep learning algorithm to estimate myocardial strain and specifically showed the relationship between the visual detection of wall motion abnormalities and defects in segmental myocardial strain. These wall motion abnormalities may be evident even at rest in patients with ischemic heart disease but can be accentuated and more evident with pharmacologic or exercise stress. We observed high agreement (Cohen κ, 0.60–0.78) between the algorithm and four expert subspecialty radiologists. While expert visual assessment is already the clinical reference standard for detecting wall motion abnormalities, this high level of agreement provides additional support. These values are comparable with or slightly higher than those reported in previous studies (42,43). DLSS identified wall motion abnormalities with performance comparable to a ground truth defined by the consensus average of four expert readers, with an AUC of 0.90 and accuracy of 86%. We further demonstrated additional clinical potential of DLSS beyond ischemic heart disease in exemplar patients with viral myocarditis and left bundle branch block.

Our ranges of globally averaged radial and circumferential strain in individuals without cardiac disease are comparable to those of previous studies, though it is important to note that meta-analyses have illustrated considerable variability among

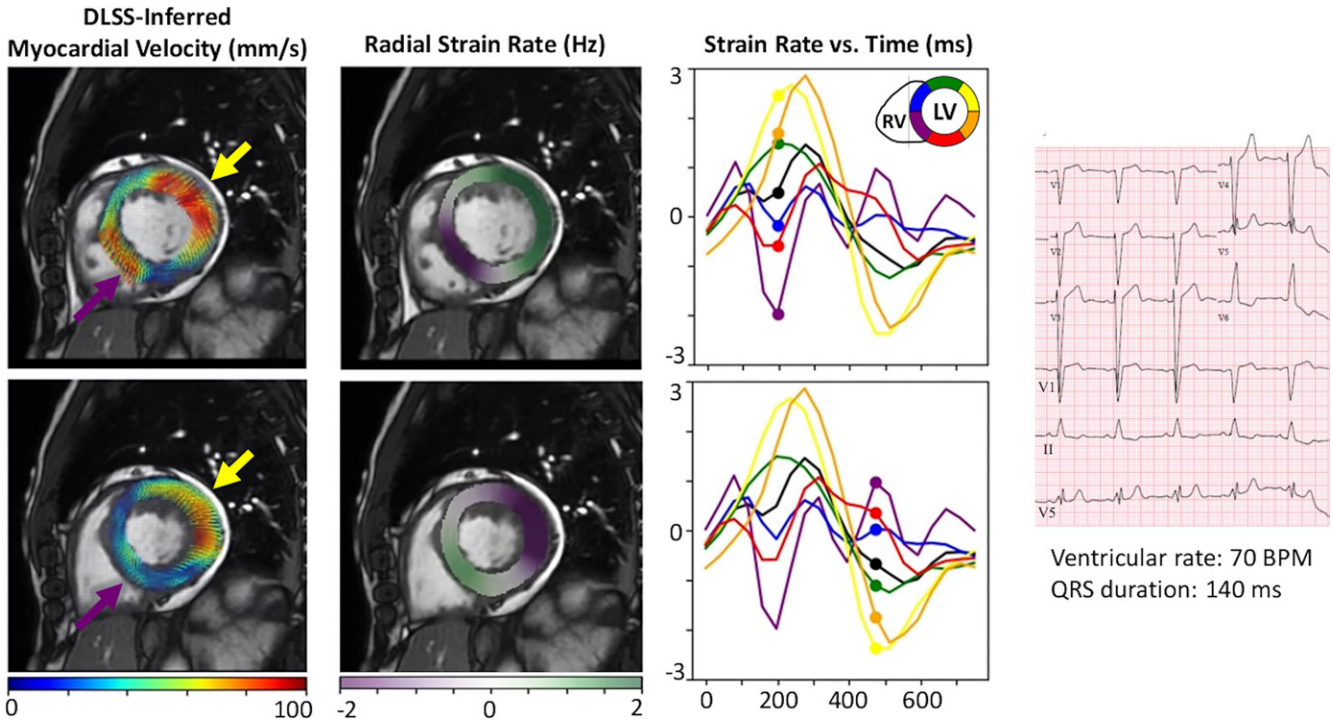

Figure 6: Images in a 54-year-old man with ventricular dyssynchrony with dissociation of contraction of the septal and lateral walls caused by left bundle branch block, visualized and quantified with deep learning synthetic strain (DLSS). Top row, left two images: MR images early in the cardiac cycle show that while the anterolateral wall (yellow arrow) contracts, the inferoseptal wall (purple arrow) relaxes. Bottom row, left two images: MR images show that the inferoseptal wall (purple arrow) then contracts while the anterolateral wall (yellow arrow) relaxes. Strain rate curves highlight the dissociation between these segments. Electrocardiogram (right) shows a left bundle branch block. BPM = beats per minute.

methods and samples of healthy individuals used in each study. A large meta-analysis comparing displacement encoding with stimulated echoes, feature tracking, and speckle tracking echocardiography found mean global radial strain in healthy individuals to be 24.3% (95% CI: 16.2%, 32.3%), 34.1% (95% CI: 28.5%, 39.7%), and 47.3% (95% CI: 43.6%, 51.0%), respectively (24). There is also wide variation of global circumferential strain in healthy participants between methods with values ranging from −17.8% (IQR: −16.4% to −19.5%) for tagging (25) to −23.4% (wide reported range of normal, up to −30%) (44) and −31.9% (95% CI: −23.1% to −40.6%) (45) for strain-encoded MRI and speckle tracking echocardiography, respectively. In our comparative analysis, DLSS and feature tracking methods showed considerable differences in strain values in individuals with normal cardiac MRI findings. However, DLSS radial strain showed greater similarity to the published literature using echocardiographic and MRI strain techniques. Moreover, reliable feature tracking for regional strain requires expert manual correction of myocardial fiducials beyond segmentation of the endocardium and epicardium for global strain (46) and is known to have considerable intervendor variability (19). Given that our deep learning method directly infers myocardial velocity from images rather than tracking individual points on the myocardial boundaries, the method requires no segmentations or manual interventions for measurement of regional strain, permitting rapid and user-independent measurements. While feature tracking has shown good reproducibility and interobserver agreement for global strain, it is less reliable for regional strain (47,48). It is important to note that DLSS was implemented with a single multitask CNN that fully addressed the inference of pixelwise myocardial motion and its quantification as a complete end-to-end solution. This multitasking strategy allowed us to train this algorithm with only a few hundred MRI examinations spanning a variety of clinical indications. A few other studies have explored the potential of deep learning to estimate myocardial motion from cine SSFP images (49–53), but they required multiple CNNs to accomplish multiple component tasks.

Several study limitations should be considered. First, all training data were acquired at 3.0 T using an MRI scanner from a single vendor at our institution. However, we established normal ranges for the DLSS algorithm and evaluated its performance in a relatively broad sample of healthy volunteers and clinical patients scanned with multiple 3.0-T and 1.5-T MRI scanners, which provides evidence of broader generalizability than might be expected considering the differences in blood pool–myocardial contrast and increased off-resonance band artifacts at different field strengths. Prior works have similarly observed broader generalizability of image segmentation (32) and image enhancement (33) algorithms. Further work may be necessary to show generalizability to MRI studies from multiple vendors and across multiple institutions and to assess the test-retest reproducibility and the effect of scan parameters such as field strength. To further establish normal reference ranges of strain for the DLSS algorithm, future studies may involve tabulation of strain from broader populations that span a range of age, sex, and other demographic variables. Second, we did not directly compare DLSS performance against prospective methods of assessing regional myocardial strain, though global averages of DLSS strain measurements largely agreed with prior studies using

other methods. Direct comparisons of this and future iterations of this approach may nevertheless be helpful to explore in future investigations. Third, in our current study, we specifically sought to correlate visible wall motion abnormalities with DLSS-computed strain. With respect to coronary artery disease, future work may assess whether DLSS can also identify regions of ischemia-induced wall motion abnormalities following the application of exercise or pharmacologic stress. It is possible that deep learning algorithms trained from other sources of myocardial velocity or strain data could provide similar results. This may be another avenue of future investigation. Finally, we have shown only results for DLSS to compute in-plane strain in short-axis cine SSFP images. Future work may include extension of the deep learning approach to long-axis images for automated measurement of regional longitudinal strain and extension to the right ventricle, permitting rigorous analysis of strain using multiple imaging planes and direct comparison against echocardiographic strain.

In conclusion, computation of regional myocardial strain from cardiac MRI has traditionally required either dedicated acquisitions of strain imaging pulse sequences or substantial manual postprocessing. We show that a newly developed deep learning algorithm, trained with 4D flow MRI velocity data, can estimate regional myocardial strain and that thresholding strain measurements is comparable to subspecialty radiologists for detecting focal wall motion abnormalities. To our knowledge, this is the first automated cardiac MRI analysis algorithm that has shown utility for detecting regional wall motion abnormalities, particularly abnormalities of regional radial strain and regional circumferential strain. DLSS is distinct from previous approaches in that no fiducial markers or manual segmentations are required—instead, it performs the complex visual tasks of inferring myocardial velocity solely from anatomic image data for each frame over an entire cardiac cycle. Given its utility for fully automating the analysis of myocardial strain from historical imaging data, DLSS and similar algorithms may enable larger-scale studies to study regional myocardial strain, including disease states beyond ischemic heart disease.

Author contributions: Guarantors of integrity of entire study, **E.M.M., A.H.**; study concepts/study design or data acquisition or data analysis/interpretation, all authors; manuscript drafting or manuscript revision for important intellectual content, all authors; approval of final version of submitted manuscript, all authors; agrees to ensure any questions related to the work are appropriately resolved, all authors; literature research, **E.M.M., C.Z., L.D.H., F.R., A.H.**; clinical studies, **E.M.M., R.S.C., S.W., L.D.H., M.H., K.J., S.K., F.R., A.P.**; statistical analysis, **E.M.M., C.Z., S.K.**; and manuscript editing, **E.M.M., R.S.C., C.Z., L.D.H., M.H., K.J., S.K., F.R., A.P., A.H.**

Disclosures of conflicts of interest: **E.M.M.** Arterys has licensed and deployed the DLSS algorithm; the University of California San Diego (UCSD) School of Medicine provided travel funding to RSNA 2022 to present related material; UCSD is pursuing a nonprovisional patent for the DLSS algorithm. **R.S.C.** Support for the present manuscript from Altman Clinical and Translational Research Institute MedGap Program, payments made to author; grants or contracts from Altman Clinical and Translational Research Institute MedGap Program, payments made to author. **S.W.** No relevant relationships. **C.Z.** No relevant relationships. **L.D.H.** No relevant relationships. **M.H.** Consulting fees from Bayer; member of GE medical imaging advisory board. **K.J.** No relevant relationships. **S.K.** Deputy editor for *Radiology: Cardiothoracic Imaging*. **F.R.** No relevant relationships. **A.P.** Research grant from GE Healthcare, unrelated to this study; member of Society of Cardiovascular Magnetic Resonance Board of Trustees; received research software support from Arterys, NeoSOFT, and CircleCV, unrelated to this study. **A.H.** Co-founder of Arterys; research grant from GE Healthcare, unrelated to this study.

References

1. Rose MJ, Jarvis K, Chowdhary V, et al. Efficient method for volumetric assessment of peak blood flow velocity using 4D flow MRI. J Magn Reson Imaging 2016;44(6):1673–1682.
2. Malayeri AA, Johnson WC, Macedo R, Bathon J, Lima JAC, Bluemke DA. Cardiac cine MRI: quantification of the relationship between fast gradient echo and steady-state free precession for determination of myocardial mass and volumes. J Magn Reson Imaging 2008;28(1):60–66.
3. La Gerche A, Claessen G, Van de Bruaene A, et al. Cardiac MRI: a new gold standard for ventricular volume quantification during high-intensity exercise. Circ Cardiovasc Imaging 2013;6(2):329–338.
4. Koch R, Lang RM, Garcia MJ, et al. Objective evaluation of regional left ventricular wall motion during dobutamine stress echocardiographic studies using segmental analysis of color kinesis images. J Am Coll Cardiol 1999;34(2):409–419.
5. Sharir T, Berman DS, Waechter PB, et al. Quantitative analysis of regional motion and thickening by gated myocardial perfusion SPECT: normal heterogeneity and criteria for abnormality. J Nucl Med 2001;42(11):1630–1638.
6. Lang RM, Bierig M, Devereux RB, et al. Recommendations for chamber quantification: a report from the American Society of Echocardiography's Guidelines and Standards Committee and the Chamber Quantification Writing Group, developed in conjunction with the European Association of Echocardiography, a branch of the European Society of Cardiology. J Am Soc Echocardiogr 2005;18(12):1440–1463.
7. Flachskampf FA, Schmid M, Rost C, Achenbach S, DeMaria AN, Daniel WG. Cardiac imaging after myocardial infarction. Eur Heart J 2011;32(3):272–283.
8. West AM, Kramer CM. Cardiovascular magnetic resonance imaging of myocardial infarction, viability, and cardiomyopathies. Curr Probl Cardiol 2010;35(4):176–220.
9. Jahnke C, Nagel E, Gebker R, et al. Prognostic value of cardiac magnetic resonance stress tests: adenosine stress perfusion and dobutamine stress wall motion imaging. Circulation 2007;115(13):1769–1776.
10. Roditi GH, Hartnell GG, Cohen MC. MRI changes in myocarditis—evaluation with spin echo, cine MR angiography and contrast enhanced spin echo imaging. Clin Radiol 2000;55(10):752–758.
11. Gandjbakhch E, Redheuil A, Pousset F, Charron P, Frank R. Clinical diagnosis, imaging, and genetics of arrhythmogenic right ventricular cardiomyopathy/dysplasia: JACC state-of-the-art review. J Am Coll Cardiol 2018;72(7):784–804.
12. Zerhouni EA, Parish DM, Rogers WJ, Yang A, Shapiro EP. Human heart: tagging with MR imaging—a method for noninvasive assessment of myocardial motion. Radiology 1988;169(1):59–63.
13. Auger DA, Zhong X, Epstein FH, Spottiswoode BS. Mapping right ventricular myocardial mechanics using 3D cine DENSE cardiovascular magnetic resonance. J Cardiovasc Magn Reson 2012;14(1):4.
14. Korosoglou G, Gitsioudis G, Voss A, et al. Strain-encoded cardiac magnetic resonance during high-dose dobutamine stress testing for the estimation of cardiac outcomes: comparison to clinical parameters and conventional wall motion readings. J Am Coll Cardiol 2011;58(11):1140–1149.
15. Osman NF, Kerwin WS, McVeigh ER, Prince JL. Cardiac motion tracking using CINE harmonic phase (HARP) magnetic resonance imaging. Magn Reson Med 1999;42(6):1048–1060.
16. Ruh A, Sarnari R, Berhane H, et al. Impact of age and cardiac disease on regional left and right ventricular myocardial motion in healthy controls and patients with repaired tetralogy of Fallot. Int J Cardiovasc Imaging 2019;35(6):1119–1132.
17. Arai AE, Gaither CC 3rd, Epstein FH, Balaban RS, Wolff SD. Myocardial velocity gradient imaging by phase contrast MRI with application to regional function in myocardial ischemia. Magn Reson Med 1999;42(1):98–109.
18. Maret E, Todt T, Brudin L, et al. Functional measurements based on feature tracking of cine magnetic resonance images identify left ventricular segments with myocardial scar. Cardiovasc Ultrasound 2009;7(1):53.
19. Backhaus SJ, Metschies G, Zieschang V, et al. Head-to-head comparison of cardiovascular MR feature tracking cine versus acquisition-based deformation strain imaging using myocardial tagging and strain encoding. Magn Reson Med 2021;85(1):357–368.
20. Scatteia A, Baritussio A, Bucciarelli-Ducci C. Strain imaging using cardiac magnetic resonance. Heart Fail Rev 2017;22(4):465–476.
21. Mirea O, Pagourelias ED, Duchenne J, et al. Intervendor differences in the accuracy of detecting regional functional abnormalities: a report from the EACVI-ASE strain standardization task force. JACC Cardiovasc Imaging 2018;11(1):25–34.
22. Popović ZB, Benejam C, Bian J, et al. Speckle-tracking echocardiography correctly identifies segmental left ventricular dysfunction induced by scarring

in a rat model of myocardial infarction. Am J Physiol Heart Circ Physiol 2007;292(6):H2809–H2816.
23. Roes SD, Mollema SA, Lamb HJ, van der Wall EE, de Roos A, Bax JJ. Validation of echocardiographic two-dimensional speckle tracking longitudinal strain imaging for viability assessment in patients with chronic ischemic left ventricular dysfunction and comparison with contrast-enhanced magnetic resonance imaging. Am J Cardiol 2009;104(3):312–317.
24. Vo HQ, Marwick TH, Negishi K. MRI-derived myocardial strain measures in normal subjects. JACC Cardiovasc Imaging 2018;11(2 Pt 1):196–205.
25. Bucius P, Erley J, Tanacli R, et al. Comparison of feature tracking, fast-SENC, and myocardial tagging for global and segmental left ventricular strain. ESC Heart Fail 2020;7(2):523–532.
26. Wu L, Germans T, Güçlü A, Heymans MW, Allaart CP, van Rossum AC. Feature tracking compared with tissue tagging measurements of segmental strain by cardiovascular magnetic resonance. J Cardiovasc Magn Reson 2014;16(1):10.
27. Fries JA, Varma P, Chen VS, et al. Weakly supervised classification of aortic valve malformations using unlabeled cardiac MRI sequences. Nat Commun 2019;10(1):3111.
28. Xue H, Artico J, Fontana M, Moon JC, Davies RH, Kellman P. Landmark detection in cardiac MRI by using a convolutional neural network. Radiol Artif Intell 2021;3(5):e200197.
29. Blansit K, Retson T, Masutani E, Bahrami N, Hsiao A. Deep learning-based prescription of cardiac MRI planes. Radiol Artif Intell 2019;1(6):e180069.
30. Zotti C, Luo Z, Lalande A, Jodoin PM. Convolutional neural network with shape prior applied to cardiac MRI segmentation. IEEE J Biomed Health Inform 2019;23(3):1119–1128.
31. Lieman-Sifry J, Le M, Lau F, Sall S, Golden D. FastVentricle: cardiac segmentation with ENet. In: Pop M, Wright G, eds. Functional imaging and modelling of the heart. FIMH 2017. Lecture Notes in Computer Science, vol 10263. Springer, 2017; 127–138.
32. Tao Q, Yan W, Wang Y, et al. Deep learning-based method for fully automatic quantification of left ventricle function from cine MR images: a multivendor, multicenter study. Radiology 2019;290(1):81–88.
33. Masutani EM, Bahrami N, Hsiao A. Deep learning single-frame and multiframe super-resolution for cardiac MRI. Radiology 2020;295(3):552–561.
34. You S, Masutani EM, Alley MT, et al. Deep learning automated background phase error correction for abdominopelvic 4D flow MRI. Radiology 2022;302(3):584–592.
35. Ghadimi S, Auger DA, Feng X, et al. Fully-automated global and segmental strain analysis of DENSE cardiovascular magnetic resonance using deep learning for segmentation and phase unwrapping. J Cardiovasc Magn Reson 2021;23(1):20.
36. Ferdian E, Suinesiaputra A, Fung K, et al. Fully automated myocardial strain estimation from cardiovascular MRI-tagged images using a deep learning framework in the UK biobank. Radiol Cardiothorac Imaging 2020;2(1):e190032.
37. Retson TA, Masutani EM, Golden D, Hsiao A. Clinical performance and role of expert supervision of deep learning for cardiac ventricular volumetry: a validation study. Radiol Artif Intell 2020;2(4):e190064.
38. Cheng JY, Hanneman K, Zhang T, et al. Comprehensive motion-compensated highly accelerated 4D flow MRI with ferumoxytol enhancement for pediatric congenital heart disease. J Magn Reson Imaging 2016;43(6):1355–1368.
39. Koo TK, Li MY. A guideline of selecting and reporting intraclass correlation coefficients for reliability research. J Chiropr Med 2016;15(2):155–163. [Published correction appears in J Chiropr Med 2017;16(4):346.]
40. Landis JR, Koch GG. The measurement of observer agreement for categorical data. Biometrics 1977;33(1):159–174.
41. Cicchetti DV. Guidelines, criteria, and rules of thumb for evaluating normed and standardized assessment instruments in psychology. Psychol Assess 1994;6(4):284–290.
42. Hoffmann R, von Bardeleben S, ten Cate F, et al. Assessment of systolic left ventricular function: a multi-centre comparison of cineventriculography, cardiac magnetic resonance imaging, unenhanced and contrast-enhanced echocardiography. Eur Heart J 2005;26(6):607–616.
43. Paetsch I, Jahnke C, Ferrari VA, et al. Determination of interobserver variability for identifying inducible left ventricular wall motion abnormalities during dobutamine stress magnetic resonance imaging. Eur Heart J 2006;27(12):1459–1464.
44. Neizel M, Lossnitzer D, Korosoglou G, et al. Strain-encoded MRI for evaluation of left ventricular function and transmurality in acute myocardial infarction. Circ Cardiovasc Imaging 2009;2(2):116–122.
45. Sugimoto T, Dulgheru R, Bernard A, et al. Echocardiographic reference ranges for normal left ventricular 2D strain: results from the EACVI NORRE study. Eur Heart J Cardiovasc Imaging 2017;18(8):833–840.
46. Schuster A, Stahnke VC, Unterberg-Buchwald C, et al. Cardiovascular magnetic resonance feature-tracking assessment of myocardial mechanics: intervendor agreement and considerations regarding reproducibility. Clin Radiol 2015;70(9):989–998.
47. Morton G, Schuster A, Jogiya R, Kutty S, Beerbaum P, Nagel E. Inter-study reproducibility of cardiovascular magnetic resonance myocardial feature tracking. J Cardiovasc Magn Reson 2012;14(1):43.
48. Mangion K, Burke NMM, McComb C, Carrick D, Woodward R, Berry C. Feature-tracking myocardial strain in healthy adults—a magnetic resonance study at 3.0 tesla. Sci Rep 2019;9(1):3239.
49. Morales MA, van den Boomen M, Nguyen C, et al. DeepStrain: a deep learning workflow for the automated characterization of cardiac mechanics. Front Cardiovasc Med 2021;8:730316.
50. Qin C, Wang S, Chen C, Qiu H, Bai W, Rueckert D. Biomechanics-informed neural networks for myocardial motion tracking in MRI. In: Martel AL, Abolmaesumi P, Stoyanov D, et al, eds. Medical Image Computing and Computer Assisted Intervention—MICCAI 2020. Lecture Notes in Computer Science, vol 12263. Springer, 2020; 296–306.
51. Morales MA, Cirillo J, Nakata K, et al. Comparison of DeepStrain and feature tracking for cardiac MRI strain analysis. J Magn Reson Imaging 2022. 10.1002/jmri.28374. Published online July 28, 2022.
52. Morales MA, Snel GJH, van den Boomen M, et al. DeepStrain evidence of asymptomatic left ventricular diastolic and systolic dysfunction in young adults with cardiac risk factors. Front Cardiovasc Med 2022;9:831080.
53. Aikawa T, Oyama-Manabe N. Editorial for "Comparison of DeepStrain and feature tracking for cardiac MRI strain analysis". J Magn Reson Imaging 2022. 10.1002/jmri.28394. Published online August 26, 2022.